4
Modeling of the test rig set-up

On the mathematical modeling topic, much has been done aiming a better understanding of the dynamic behavior of drilling systems, as already seen in Section 2.1. Complex models with geometric nonlinearities, stochastic processes, and/or vibration coupling are used in order to analyze the system as a whole - as the phenomena happen in the field. The finite element method is largely used to achieve these complex models (see [45, 54, 59–61, 63, 94, 95]). There are authors that approach the drilling system via Delay Differential Equations like [28, 65–67, 96–100] aiming to analyze the stability and/or propose a control actuation. On the other hand, mathematical modeling via lumped parameters has also widespread use. This technique may include vibration coupling, control and stability analysis [51, 56, 101, 102], and it has presented good results compared to field data [50, 69] and experimental trials [40, 43, 48, 90, 103].

Henceforward the mathematical model is considered: in Section 4.1, the test bench is described by means of lumped parameters. Subsequently, the qualitative and quantitative comparisons are presented in order to ensure the representation of the model. Afterwards, Section 4.3 provides a discussion about the DC-motor dynamics in order to clarify its implementation. From this point, the stability analysis of the proposed and validated model is presented for the purpose of identifying equilibrium and periodic solutions in Section 4.4: herein, the Hurwitz criterion is applied to local stability analysis, followed by the bifurcation diagrams via numerical methods. The closure remarks are presented in Section 4.5.

4.1
Equations of motion

The electric subsystem is modeled as a voltage source connected in series with a resistor and an inductor, providing torque τ_m. The angular velocity $\dot{\theta}_m$ imposed by τ_m is eight times greater than the angular velocity $\dot{\theta}_3$ transmitted to the mechanical subsystem due to the transmission factor $\eta = 8:1$.

Mathematically, the electric subsystem may be expressed as

$$L\,\frac{\mathrm{d}\,i}{\mathrm{d}t} + R\,i + K_E\,\dot{\theta}_m = u, \tag{4-1a}$$

$$\tau_m = K_T\,i - C_m\,\dot{\theta}_m - T_f - J_m\,\ddot{\theta}_m, \tag{4-1b}$$

where i denotes electric current of the DC-motor. L and R are the armature inductance and resistance, respectively. The angular velocity $\dot{\theta}_m$ is the velocity of the inertia of the DC-motor J_m. C_m and K_T are the speed regulation and constant torque of the motor, respectively. Further, K_E consists of the voltage constant and T_f is the internal friction torque. The input voltage is denoted by u.

The mechanical subsystem illustrated in Figure 3.3 is mathematically written as

$$J_1\ddot{\theta}_1 + d_1\left(\dot{\theta}_1 - \dot{\theta}_2\right) + k_1\left(\theta_1 - \theta_2\right) + T_{r_1}(\dot{\theta}_1) = 0 \tag{4-2a}$$

$$J_2\ddot{\theta}_1 + d_1\left(\dot{\theta}_2 - \dot{\theta}_1\right) + d_2\left(\dot{\theta}_2 - \dot{\theta}_3\right) + k_2\left(\theta_2 - \theta_3\right) + k_1\left(\theta_2 - \theta_1\right) + T_{r_2}(\dot{\theta}_2) = 0 \tag{4-2b}$$

$$d_2\left(\dot{\theta}_3 - \dot{\theta}_2\right) + k_2\ \left(\theta_3 - \theta_2\right) = \tau_s, \tag{4-2c}$$

where J_i for $i = 1, 2$ represents the moment of inertia of each degree of freedom. The angular displacements, velocities and accelerations are denoted by θ_i, $\dot{\theta}_i$ and $\ddot{\theta}_i$ for $i = 1, 2, 3$, respectively. The relations between the subsystems are $\tau_s = \eta\,\tau_m$ and $\dot{\theta}_m = \eta\,\dot{\theta}_3$. Combining Eq. (4-1b) with Eq. (4-2c), and defining $\delta_{12} = \theta_1 - \theta_2$ and $\delta_{23} = \theta_2 - \theta_3$,

$$J_1\ddot{\theta}_1 + d_1\left(\dot{\theta}_1 - \dot{\theta}_2\right) + k_1\delta_{12} + T_{r_1}(\dot{\theta}_1) = 0 \tag{4-3a}$$

$$J_2\ddot{\theta}_1 + d_1\left(\dot{\theta}_2 - \dot{\theta}_1\right) + d_2\left(\dot{\theta}_2 - \dot{\theta}_3\right) + k_2\delta_{23} - k_1\delta_{12} + T_{r_2}(\dot{\theta}_2) = 0 \tag{4-3b}$$

$$d_2\left(\dot{\theta}_3 - \dot{\theta}_2\right) - k_2\delta_{23} = \eta\left(K_T\,i - C_m\eta\,\dot{\theta}_3 - T_f - J_m\eta\,\ddot{\theta}_3\right) \tag{4-3c}$$

$$L\,\frac{\mathrm{d}\,i}{\mathrm{d}t} + R\,i + K_E\,\eta\,\dot{\theta}_3 = u. \tag{4-3d}$$

The stiffnesses are denoted by k_1 and k_2, as well as d_1 and d_2 denote the damping. The first (k_1 and d_1) correspond to the stiffness and damping between R_1 and R_2, while the second (k_2 and d_2) represent the stiffness and damping between R_2 and R_3 (see Figure 3.3). From Eq. (4-3), the system may be rewritten as state space formulation in order to be integrated using *VODE* integrator ('bdf' method) from `Python`. The following Eqs. (4-4) and (4-5) show the state variables and state equations, respectively

$$\mathbf{x} = \begin{bmatrix} \theta_1 - \theta_2 \\ \theta_2 - \theta_3 \\ \dot{\theta}_1 \\ \dot{\theta}_2 \\ \dot{\theta}_3 \\ i \end{bmatrix} = \begin{bmatrix} x_1 \\ x_2 \\ x_3 \\ x_4 \\ x_5 \\ x_6 \end{bmatrix}, \tag{4-4}$$

$$\dot{x}_1 = x_3 - x_4 \tag{4-5a}$$
$$\dot{x}_2 = x_4 - x_5 \tag{4-5b}$$
$$\dot{x}_3 = \left[-d_1 x_3 + d_1 x_4 - k_1\, x_1 - T_{r_1}(x_3)\right]/J_1 \tag{4-5c}$$
$$\dot{x}_4 = \left[d_1 x_3 - (d_1 + d_2) x_4 - d_2 x_5 + k_1\, x_1 - k_2\, x_2 - T_{r_2}(x_4)\right]/J_2 \tag{4-5d}$$
$$\dot{x}_5 = \left[k_2\, x_2 - (\eta^2 C_m + d_2) x_5 + d_2 x_4 + \eta K_T\, x_6 - \eta T_f\right]/J_3 \tag{4-5e}$$
$$\dot{x}_6 = \left[-R\, x_6 - \eta K_E\, x_5 + u\right]/L, \tag{4-5f}$$

where $J_3 = \eta^2\, J_m$. As described in Chapter 3, the DC-motor presents a PI internal controller which is responsible to maintain the angular velocity of the motor. Herein, this input voltage may be expressed as

$$u = k_p\, (\omega_{ref} - x_5) + k_i \int_0^t (\omega_{ref} - x_5)\, \mathrm{d}t \tag{4-6}$$

where k_p and k_i are the proportional and integral constants, ω_{ref} is the reference angular velocity in rad/s. This relation in Eq. (4-6) maintains the idea of a desired angular speed that is imposed by an operator.

Following, the resistive torque is expressed as Eq. (3-13). This equation may be rewritten as

$$T_{r_1}(\dot{\theta}_1) = N_1\, r_1\, \left[\mu_k + (\mu_s - \mu_k) \cdot e^{-\mathrm{v_b}|\dot{\theta}_1|}\right] \cdot \mathrm{sign}\left(\dot{\theta}_1\right), \tag{4-7}$$

where N_1 and r_1 are the normal force and distance between the contact point and the rotation center of the disc R_1. The static and kinetic friction coefficients are represented by μ_s and μ_k, respectively. The parameter $\mathrm{v_b}$ represents the decay factor. Herein, the sign $\left(\dot{\theta}_1\right)$ is defined as

$$\operatorname{sign}\left(\dot{\theta}_1\right) = \begin{cases} 1 & for \quad \dot{\theta}_1 \geq 0 \\ -1 & for \quad \dot{\theta}_1 < 0 \end{cases} . \tag{4-8}$$

To solve Eq. (4-5) numerically while avoiding the discontinuity of Eq. (4-7) one needs to rewrite the last one as follows [70]

$$T_{r_1}(\dot{\theta}_1) = N_1\, r_1 \begin{cases} \mu_s\, \dot{\theta}_1/\omega_s & for \quad |\dot{\theta}_1| < \omega_s \\ \left[\mu_k + (\mu_s - \mu_k)\cdot e^{-\mathrm{v_b}|\dot{\theta}_1|}\right]\cdot \operatorname{sign}\left(\dot{\theta}_1\right) & for \quad |\dot{\theta}_1| \geq \omega_s \end{cases} , \tag{4-9}$$

where $\omega_s = 10^{-3}$ and $\mathrm{v_b} = 1$. Figure 4.1(a) depicts the discontinuous model of the dependent-velocity friction, whereas Figure 4.1(b) illustrates the model to avoid the discontinuity as expressed in Eq. (4-9).

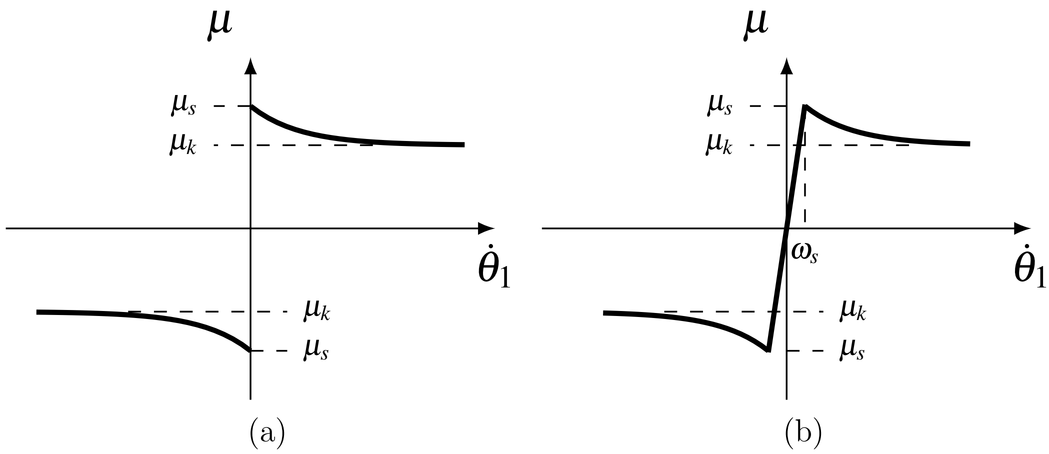

Figure 4.1: Graphic representation of (a) the discontinuous friction model and (b) the adopted friction model.

4.2 Model validation

Briefly, a model validation aims to assess the mathematical model by comparing its outputs with experimental measurements and then the dynamic behavior predictions may be conducted [83]. Once the characterization of the experimental apparatus had been performed (see Chapter 3), it is possible to provide the needed parameters to the mathematical model described in the previous section. The mechanical and electrical parameters are presented in Tables 3.1 and 4.1.

Therewith, the qualitative and quantitative validation are addressed in order to verify the correlation between numerical and experimental results. This procedure illustrates and ensures that the mathematical modeling corresponds to the drill-string experimental set-up.

Table 4.1: Mechanical parameters of test rig.

Parameter	**Description**	**Value**	**Unit**
J_1	R_1 moment of inertia	0.0288	kgm^2
J_2	R_2 moment of inertia	0.0149	kgm^2
J_3	DC-motor moment of inertia	0.0237	kgm^2
k_1	stiffness between R_1-R_2	1.1175	Nm/rad
k_2	stiffness between R_2-Motor	0.3659	Nm/rad
d_1	damping between R_1-R_2	0.0202	Nms/rad
d_2	damping between R_2-Motor	0.0167	Nms/rad
μ_s	static friction coefficient	0.500	−
μ_k	kinetic friction coefficient	0.306	−
$\mathrm{v_b}$	decay factor	1.000	s/rad

– *Qualitative comparison.* Qualitative comparisons may be roughly described as binary results, *e.g.* positive/negative results. For this analysis, the voltage relating to 3.14 rad/s and 4.19 rad/s (30 and 40 rpm) was imposed on the DC-motor, thus the angular velocities of the model were compared with experimental data. Figures 4.2 and 4.3 depict the numerical and experimental data, where the numerical results present a similar behavior of the acquired data.

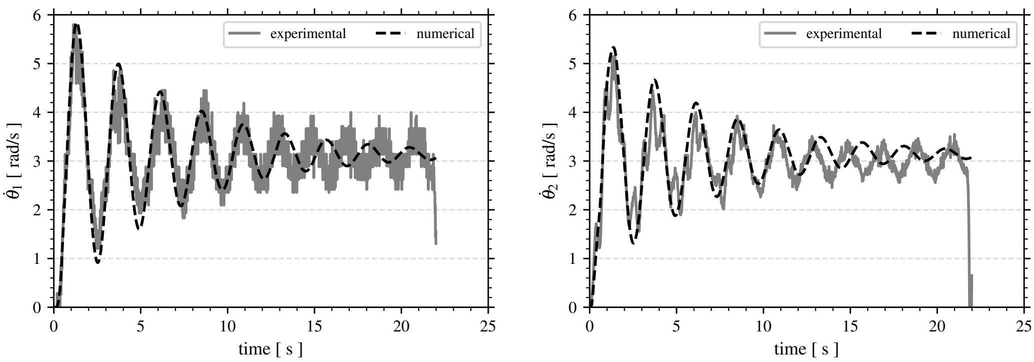

(a) (b)

Figure 4.2: Numerical and experimental angular velocity of (a) R_1 and (b) R_2 for 3.14 rad/s (30 rpm). Continuous gray and dashed black lines contain experimental and numerical results respectively.

– *Quantitative comparison.* Quantitatively, the numerical model also presented very matched results. According to [104], the *Correlation Method* is widely used for its easy implementation. This method (Pearson correlation coefficient) consists of the Eq. (4-10)

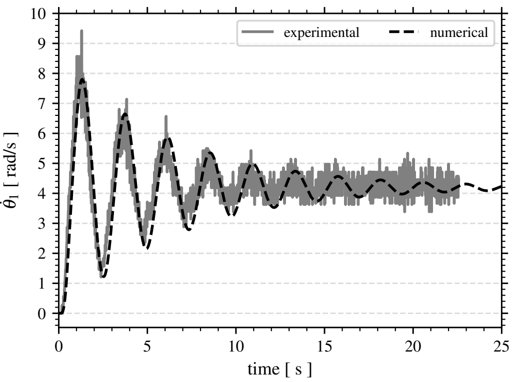

(a)

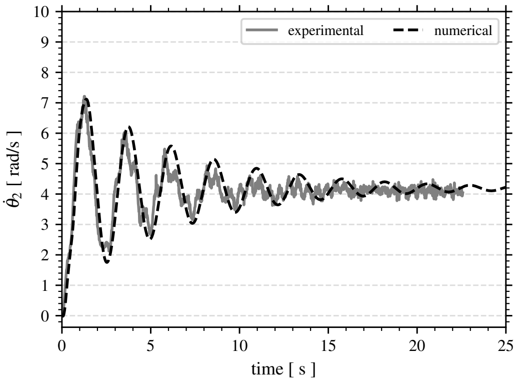

(b)

Figure 4.3: Numerical and experimental angular velocity (a) $\dot{\theta}_1$ and (b) $\dot{\theta}_2$ for 4.19 rad/s (40 rpm). Continuous gray and dashed black lines contain experimental and numerical results respectively.

$$P_C = \frac{\sum_{i=0}^{n} X_{1_i} \cdot X_{2_i} - \frac{\sum_{i=0}^{n} X_{1_i} \cdot \sum_{i=0}^{n} X_{2_i}}{n}}{\sqrt{\left(\sum_{i=0}^{n} X_{1_i}^2 - \frac{\left(\sum_{i=0}^{n} X_{1_i}\right)^2}{n}\right) \cdot \left(\sum_{i=0}^{n} X_{2_i}^2 - \frac{\left(\sum_{i=0}^{n} X_{2_i}\right)^2}{n}\right)}}, \tag{4-10}$$

where X_{1_i} and X_{2_i} are data of the experimental and numerical models, and n is the number of points. If P_C is equal to 1 means a perfect match between experimental and numerical data. Otherwise, $P_C = 0$ means a total mismatch between data. It is important to remark that this correlation coefficient is applied only in the first 10 seconds.

Another indicator is the *Amplitude Pulse Level (APL)* which measures the difference between the data maximum amplitudes [104]. This is quantified as

$$APL = \frac{|\max(X_1) - \max(X_2)|}{|\max(X_1)|}. \tag{4-11}$$

In this indicator, $APL = 0$ means a perfect match whereas $APL = 1$ means a total mismatch. In Table 4.2 it is shown the validation method indicators expressed by Eqs. (4-10) and (4-11) for the angular velocity $\dot{\theta}_1$ of the experimental and numerical results.

– Stick-slip comparison. Moreover, the behavior during stick-slip of the system is compared (see Figure 4.4). In Figure 4.4(a), one may observe the increasing phase loss between the amplitude oscillations of the numerical and experimental models. After nearly 10 peaks, the numerical and experimental results match again. This behavior may be linked to nonlinear phenomena that are not modeled by the friction model.

Table 4.2: Quantitative comparison between experimental and numerical of $\dot{\theta}_1$.

ω_{ref} $[rpm]$	P_C $[-]$	APL $[-]$
30	0.898	0.010
40	0.893	0.172
50	0.941	0.114
70	0.955	0.119

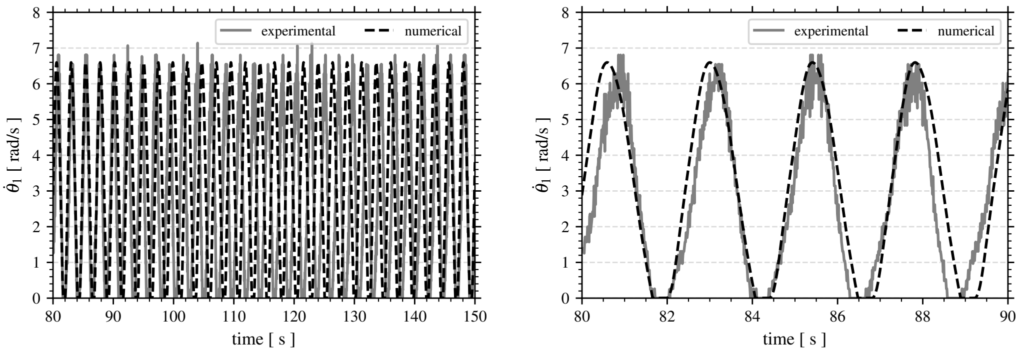

(a) (b)

Figure 4.4: Test rig response for 3.14 rad/s (30 rpm) with (a) stick-slip and (b) stick-slip zoomed. N_1 = 25.0 N and T_{r_2} = 0.0 Nm. Continuous gray and dashed black lines contain experimental and numerical results, respectively.

Nevertheless, the stick time (which means the time during the stick phase [82]) and the amplitude of oscillations are similar.

4.3 DC-motor dynamics

Several authors do not consider the motor dynamics. Usually, they state that there is a torque source strong enough to provide constant velocity at the top end. Other authors add a small harmonic term to the top end speed, aiming to emulate the motor dynamics.

The DC-motor described in Section 3.1 is not strong enough and the mechanical subsystem behavior may influence the DC-motor dynamics. Figure 4.5 depicts the free transient oscillations after imposing a step signal of the reference angular velocity ω_{ref}. One may note that the numerical results did not depict the oscillation amplitude but it oscillates nearly in the same frequency. This may happen because the DC-motor is old and therefore these parameters may not match to the actual ones.

In Figure 4.6 the experimental angular velocities of Disc 1, Disc 2, and DC-motor are shown: the reference angular velocity ω_{ref} = 3.0 rad/s is imposed; then a normal force N_1 is applied at R_1 (in 8 s) in order to induce

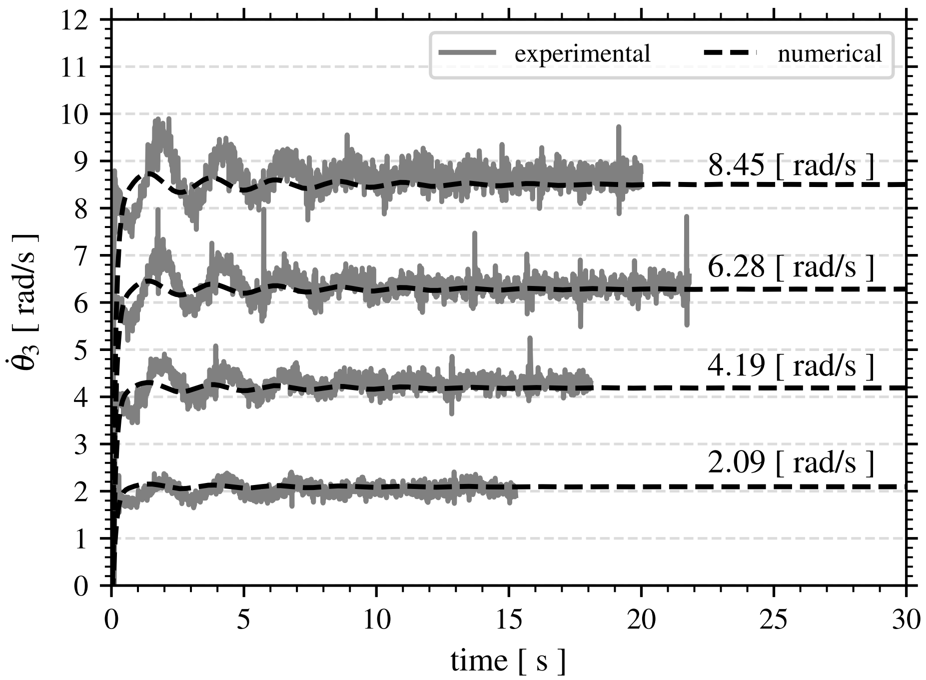

Figure 4.5: Free oscillations of the angular velocity of the DC- motor $\dot{\theta}_3$ for different reference velocities. Continuous gray and dashed black lines contain experimental and numerical results, respectively.

stick-slip; thereafter, the N_1 is removed (in 46 s). One may easily observe that the angular velocity of the DC-motor is not constant during stick-slip phenomenon. Further, $\dot{\theta}_3$ presents fluctuations around an angular speed slightly lower than the reference speed ω_{ref}. This latter figure illustrates the influence of the mechanical subsystem on the electrical subsystem. Here the adopted DC-motor model does not present this behavior.

Numerically, the angular velocity of Disc 1 ($\dot{\theta}_1$) and the armature current are illustrated in Figure 4.7. The stick-slip phenomenon is observed from time $t = 50$ s, when $N_1 = 25.0$ N is applied. In the same time, the armature current presents large oscillations during torsional vibrations.

4.4 Stability analysis

The qualitative structure of the dynamic flow can change when certain parameters vary. Therewith, stable solutions can be created or destroyed, or become unstable. Then, the stability analysis is important to identify changes in behavior of the system when some bifurcation parameter varies [105–108].

Stable equilibrium points or trajectories (all discs with the same angular velocity ω_{ref}) and stable limit cycles (torsional vibration at the discs) were observed in the experimental set-up. Thereby, these behavior sets are

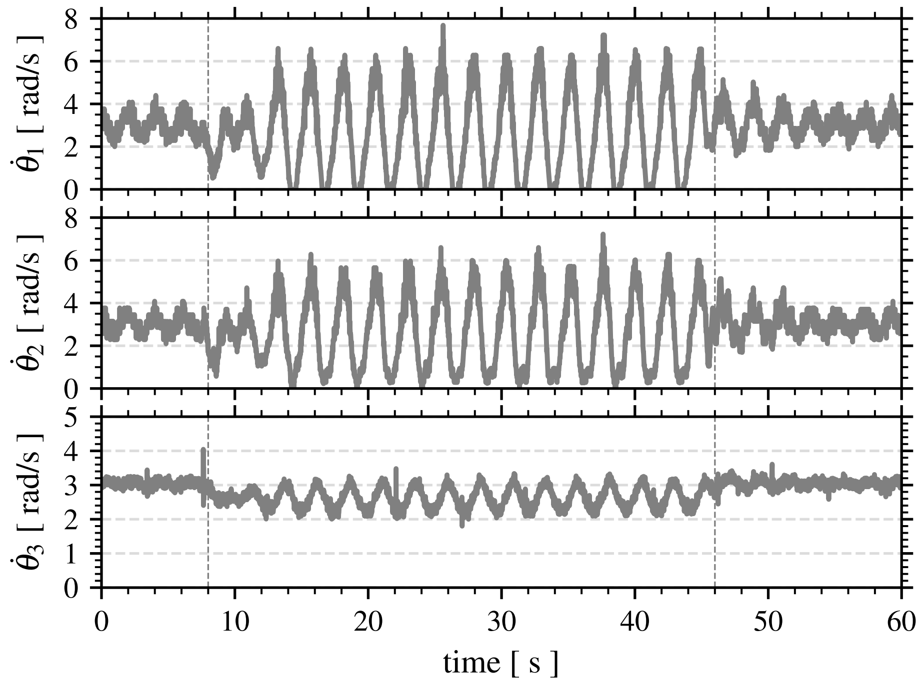

Figure 4.6: Experimental angular velocities of Disc 1, Disc 2, and DC-motor for $\omega_{ref} = 3.0\ rad/s$.

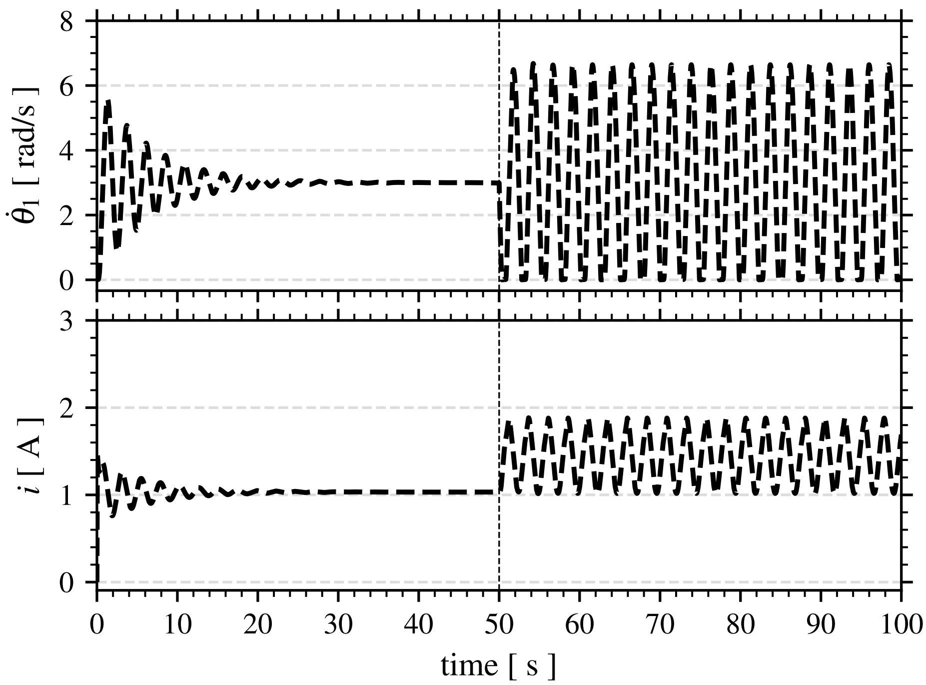

Figure 4.7: Numerical angular velocity of Disc R_1 and the armature current i of the DC-motor. For time $t < 50\ s$, $N_1 = 0.0$ N; for time $t \geq 50\ s$, $N_1 = 25$ N. Reference speed is $\omega_{ref} = 3.0\ rad/s$.

approached in this section.

4.4.1
Equilibrium points

Remind that the test bench system described by Eq. (4-3) presents nonlinearities rising from the friction torque model on R_1, and at the moment, there is no torque applied on Disc 2 (R_2), so that $T_{r_2} = 0.0$ Nm. For the analytical and stability analysis, the resistive torque described by Eq. (4-7) is used.

Therewith, in the equilibrium points it holds that $\left(\delta_{12}, \delta_{23}, \dot{\theta}_1, \dot{\theta}_2, \dot{\theta}_3, i\right) = (\delta_{12}^*, \delta_{23}^*, \omega^*, \omega^*, \omega^*, i^*)$ and $u = u_c$ so that u_c is a constant. Also, $\delta_{12} = \theta_1 - \theta_2$ and $\delta_{23} = \theta_2 - \theta_3$. Thereby, Eq. (4-3) becomes

$$k_1\, \delta_{12}^* + T_{r_1}(\omega^*) = 0, \tag{4-12a}$$

$$k_2\, \delta_{23}^* - k_1\, \delta_{12}^* = 0, \tag{4-12b}$$

$$C_m \eta^2\, \omega^* - k_2\, \delta_{23}^* = \eta K_T\, i^* - \eta T_f, \tag{4-12c}$$

$$R\, i^* + \eta K_E\, \omega^* = u_c. \tag{4-12d}$$

Equation (4-12c) means a torque balance of the electro-mechanical system:

$$C_m \eta^2\, \omega^* + T_{r_1}(\omega^*) + \eta T_f = \eta K_T\, i^*, \tag{4-13}$$

where the right side means the provided torque and the left side the loss torques. Also, one may verify the equilibrium point as

$$\begin{array}{rcl} \delta_{12}^* & = & \frac{-T_{r_1}(\omega_1^*)}{k_1}, \\ \delta_{23}^* & = & \frac{-T_{r_1}(\omega^*)}{k_2}, \\ i^* & = & \frac{u_c - \eta K_E\, \omega^*}{R}. \end{array} \tag{4-14}$$

Herein, two possibilities may be considered:

1. equilibrium for $\omega^* = 0$, i.e., all discs stand still; and
2. equilibrium for $\omega^* \neq 0$ and all discs present the same angular velocity such as $\omega^* = \omega_{ref}$.

At this point, the input voltage law given by Eq. (4-6) is recalled, and the time dependent term is unconsidered. The system lies on Case 1 if $\omega_{ref} \leq \omega_{min}$ such that

$$\omega_{min} = \frac{(T_{r_{1s}} + \eta\, T_f)\; R}{\eta\, K_T\, k_p}, \tag{4-15}$$

where $T_{r_{1s}} = N_1 \, r_1 \, \mu_s$. This means that for $\omega_{ref} \leq \omega_{min}$, the DC-motor does not provide enough torque to overcome the losses and the system remains still.

The other case concerns all discs with the same angular velocity $\left(\dot{\theta}_1 = \dot{\theta}_2 = \dot{\theta}_2 = \omega_{ref}\right)$. Therewith,

$$\begin{aligned} \delta_{12}^* &= \tfrac{-T_{r_1}(\omega_{ref})}{k_1} \\ \delta_{23}^* &= \tfrac{-T_{r_1}(\omega_{ref})}{k_2} \\ i^* &= \tfrac{\eta^2 C_m \, \omega_{ref} + T_{r_1}(\omega_{ref}) + \eta T_f}{\eta K_T}. \end{aligned} \tag{4-16}$$

Equation (4-16) represents the desired situation: the system rotates with an imposed and constant angular velocity ω_{ref}.

4.4.2
Local stability analysis

In order to analyze the local stability for $\omega_{ref} > \omega_{min}$, the system is linearized around an equilibrium point. First, Eq. (4-5) is rewritten as follows

$$\begin{aligned} &\dot{x}_1 = x_3 - x_4 \\ &\dot{x}_2 = x_4 - x_5 \\ &\dot{x}_3 = \left[-d_1 x_3 + d_1 x_4 - k_1 \, x_1 - T_{r_1}(x_3)\right] / J_1 \\ &\dot{x}_4 = \left[d_1 x_3 - (d_1 + d_2) x_4 - d_2 x_5 + k_1 \, x_1 - k_2 \, x_2 - T_{r_2}(x_4)\right] / J_2 \\ &\dot{x}_5 = \left[k_2 \, x_2 - (\eta^2 C_m + d_2) x_5 + d_2 x_4 + \eta K_T \, x_6 - \eta T_f\right] / J_3 \\ &\dot{x}_6 = \left[-R \, x_6 - \eta K_E \, x_5 + k_p \, (\omega_{ref} - x_5) + k_i \, x_7\right] / L, \\ &\dot{x}_7 = \omega_{ref} - x_5. \end{aligned} \tag{4-17}$$

Equation (4-17) contains the internal PI controller of the DC-motor and the error ($\dot{x}_7 = \omega_{ref} - x_5$) is a state of the system. The Jacobian matrix around an equilibrium $\mathbb{J}^*$ is defined as

$$\mathbb{J}^* = \left[\frac{\partial \dot{x}_i}{\partial x_j}\right] \tag{4-18}$$

for $i, j = 1, \cdots, 7$, and then $\mathbb{J}^*$ may be written as

$$\mathbb{J}^* = \begin{bmatrix} 0 & 0 & 1 & -1 & 0 & 0 & 0 \\ 0 & 0 & 0 & 1 & -1 & 0 & 0 \\ \mathbb{J}_{31} & 0 & \mathbb{J}_{33} & \mathbb{J}_{34} & 0 & 0 & 0 \\ \mathbb{J}_{41} & \mathbb{J}_{42} & \mathbb{J}_{43} & \mathbb{J}_{44} & \mathbb{J}_{45} & 0 & 0 \\ 0 & \mathbb{J}_{52} & 0 & \mathbb{J}_{54} & \mathbb{J}_{55} & \mathbb{J}_{56} & 0 \\ 0 & 0 & 0 & 0 & \mathbb{J}_{65} & \mathbb{J}_{66} & \mathbb{J}_{67} \\ 0 & 0 & 0 & 0 & -1 & 0 & 0 \end{bmatrix} \tag{4-19}$$

where

$$
\begin{aligned}
\mathbb{J}_{31} &= \tfrac{-k_1}{J_1}, & \mathbb{J}_{33} &= \tfrac{1}{J_1}\left[-\Delta T_{r_1} - d_1\right],\\
\mathbb{J}_{34} &= \tfrac{d_1}{J_1}, & \mathbb{J}_{41} &= \tfrac{k_1}{J_2},\\
\mathbb{J}_{42} &= \tfrac{-k_2}{J_2}, & \mathbb{J}_{43} &= \tfrac{d_1}{J_2},\\
\mathbb{J}_{44} &= \tfrac{1}{J_2}\left[-d_1 - d_2\right], & \mathbb{J}_{45} &= \tfrac{d_2}{J_2},\\
\mathbb{J}_{52} &= \tfrac{-k_2}{J_3}, & \mathbb{J}_{54} &= \tfrac{d_2}{J_3},\\
\mathbb{J}_{55} &= -\tfrac{1}{J_3}\left[\eta^2 C_m + d_2\right], & \mathbb{J}_{56} &= \tfrac{\eta K_T}{J_3},\\
\mathbb{J}_{65} &= \tfrac{-\eta K_E - k_p}{L}, & \mathbb{J}_{66} &= \tfrac{-R}{L},\\
\mathbb{J}_{67} &= \tfrac{k_i}{L}.
\end{aligned}
\tag{4-20}
$$

Equation (4-20) contains the ΔT_{r_1} that represents the friction damping [44] at discs R_1 provided by the restive torque, i.e.,

$$
\Delta T_{r_1} = \left.\frac{\mathrm{d}T_{r_1}}{\mathrm{d}\dot{\theta}_1}\right|_{\dot{\theta}_1=\omega^*}. \tag{4-21}
$$

The characteristic polynomial of the matrix $\mathbb{J}^*$ is presented as follows

$$
\lambda^7 + a_1\lambda^6 + a_2\lambda^5 + a_3\lambda^4 + a_4\lambda^3 + a_5\lambda^2 + a_6\lambda + a_7 = 0 \tag{4-22}
$$

Therewith, the Hurwitz criterion is applied. This criterion states that a characteristic equation will have only eigenvalues with the negative real part if the coefficients are nonzero and the Hurwitz matrix has positive minors Δ_i (for $i = 1, 2, \cdots, 7$) [109], *i.e.*, $\Delta_i > 0$. The $\mathbb{H}$ matrix may be written as

$$
\mathbb{H} = \begin{bmatrix}
a_1 & a_3 & a_5 & a_7 & 0 & 0 & 0\\
1 & a_2 & a_4 & a_6 & 0 & 0 & 0\\
0 & a_1 & a_3 & a_5 & a_7 & 0 & 0\\
0 & 1 & a_2 & a_4 & a_6 & 0 & 0\\
0 & 0 & a_1 & a_3 & a_5 & a_7 & 0\\
0 & 0 & 1 & a_2 & a_4 & a_6 & 0\\
0 & 0 & 0 & a_1 & a_3 & a_5 & a_7
\end{bmatrix}. \tag{4-23}
$$

The characteristic polynomial coefficients and the principal minors are described in Appendix A.

Herein, all the Δ_i are polynomials as functions of ΔT_{r_1}. Therefore, one may state that the equilibrium point of the system is asymptotically stable for

$$
\Delta T_{r_1} > \Delta T_{r_{min}} \tag{4-24}
$$

where $\Delta T_{r_{min}} = \max(\Delta T_{\Delta_i})$, and ΔT_{Δ_i} is the largest real part of the roots of the polynomial Δ_i for $i = 1, 2, ..., 7$. For the system parameters presented in Tables 3.1 and 4.1, one obtains

$$\Delta T_{r_{min}} = -0.0128 \quad \frac{Nms}{rad}. \tag{4-25}$$

Figure 4.8(a) illustrates the following case: $N_1 = 10.0$ N, the system is locally stable for $\dot{\theta}_1 > 1.994$ rad/s. For $\dot{\theta}_1 < 1.994$ rad/s, the stability is not ensured. In addition, Figure 4.8(b) shows the case that $N_1 = 20.0$ N, the system is locally stable for $\dot{\theta}_1 > 2.689$ rad/s, and for $\dot{\theta}_1 < 2.689$ rad/s, the system is unstable, according to Hurwitz criterion. As one may also verify in Figure 4.8, the negative slope of the friction model may be crucial to the stable solution.

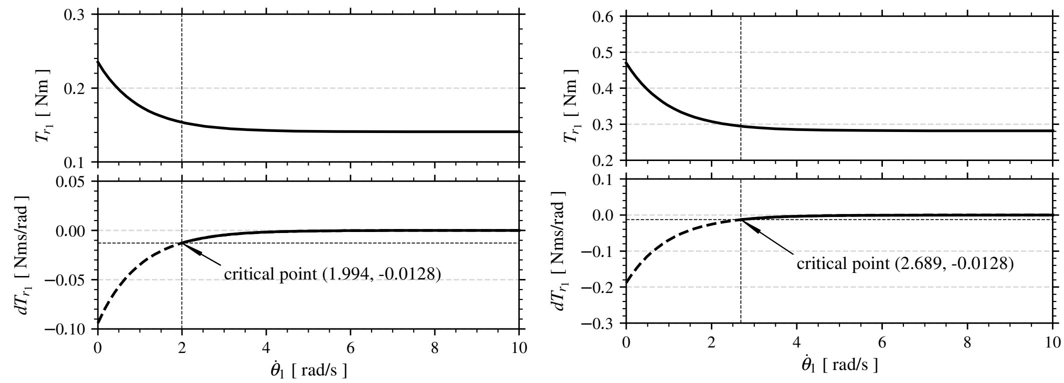

(a) (b)

Figure 4.8: Graphic illustration of the local stability analysis via Hurwitz criterion for (a) $N_1 = 10.0$ N, and (b) $N_1 = 20.0$ N. Continuous and dashed lines mean asymptotically local stable and unstable, respectively.

Using the performed stability analysis so far, the equilibrium set expressed by Eq. (4-16) is illustrated in Figure 4.9. Before the minimum angular velocity $\omega_{ref} < \omega_{min}$ given by Eq. (4-15), there exists a stable equilibrium branch which means that the system remains still (not enough torque to overcome the losses). Thereafter, the equilibrium branch becomes locally unstable. For speeds above the critical velocity observed in Figure 4.8, the equilibrium branch becomes stable again.

Furthermore, Figures 4.8 and 4.9 may provide the bifurcation type occurring at $\omega_{ref} = \omega_c$, where ω_c represents the critical (limit) value of the bifurcation parameter. Replacing the limit values into, one may conclude that the system passes through a Hopf bifurcation (or Andronov-Hopf bifurcation), meeting the needed conditions for this [105, 107, 110]. Figure 4.10 exhibits a conjugate eigenvalue of the Jacobian matrix (Eq. (4-19)) crossing the imaginary axis of the complex plane [44, 105–107, 110].

The torsional vibration map (TVM) may also be obtained via Hurwitz criterion [20, 109, 111]. Figure 4.11(a) illustrates two zones: one with stable periodic solutions and the other with equilibrium solutions [105]. This means

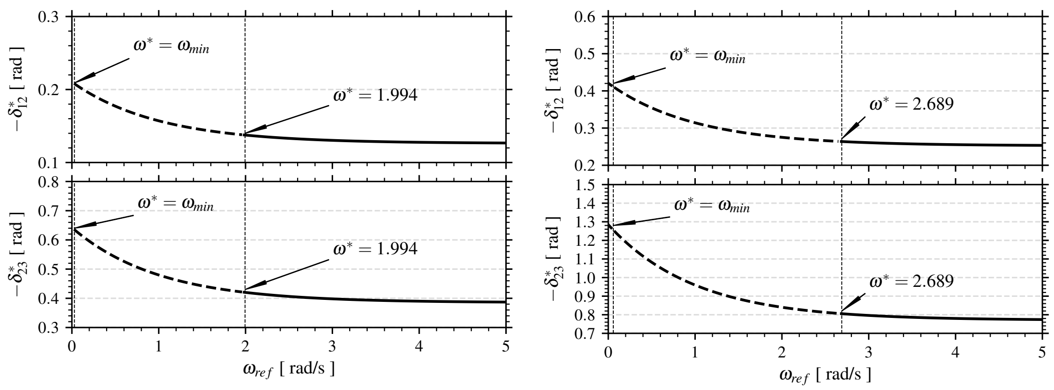

(a) (b)

Figure 4.9: Local stability analysis of the equilibrium branch (Eq. 4-16) via Hurwitz criterion for (a) $N_1 = 10.0$ N, and (b) $N_1 = 20.0$ N. Continuous and dashed lines mean locally stable and unstable branches, respectively.

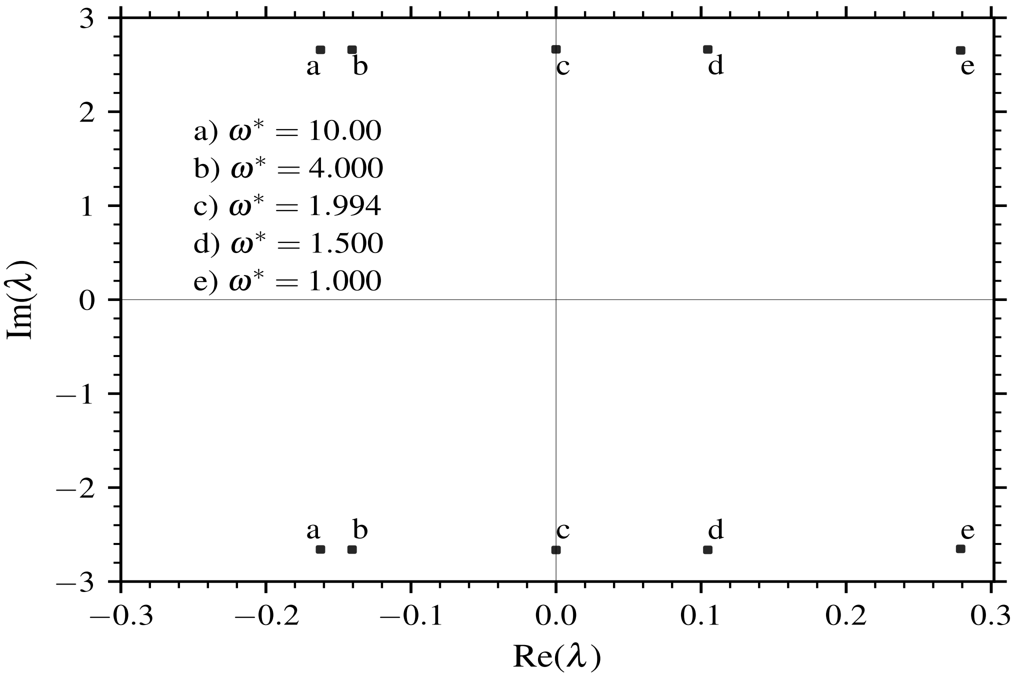

Figure 4.10: Imaginary-axis crossing of a conjugate eigenvalue of the Jacobian matrix for different values of ω^* (in rad/s) and $N1 = 10.0$ N.

that in the left side of the curve, the system undergoes torsional vibrations (upper Figure 4.11(b)) and, in the right side, it presents no vibration (lower Figure 4.11(b)).

4.4.3 Bifurcation diagrams

As experimentally observed in previous sections, the system performs equilibrium and periodic solutions depending on the reference angular velocity

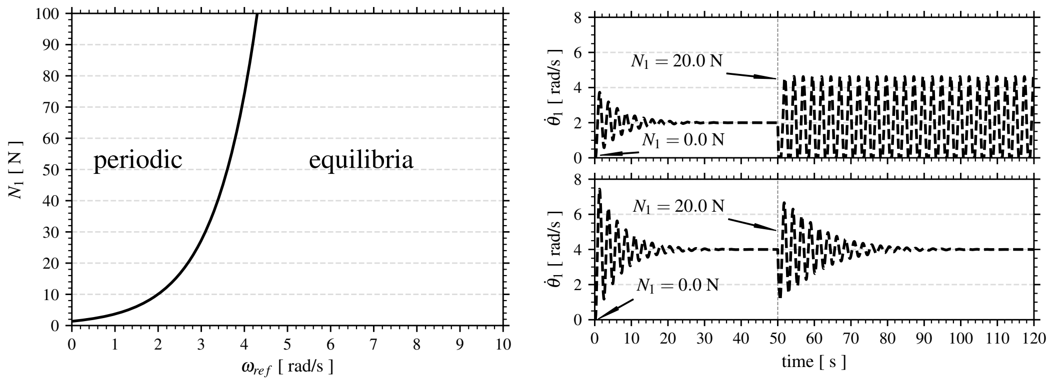

(a) (b)

Figure 4.11: (a) Torsional vibration map and (b) time response of the Disc 1 (R_1) for 2 rad/s (upper) and 4 rad/s (lower). $N_1 = 0.0$ N at $0 < t < 50$ and $N_1 = 20.0$ N at $t > 50$.

ω_{ref}. Therewith, this imposed parameter is chosen as the bifurcation parameter for the analysis. The limit cycles and equilibria are numerically obtained via `PyDSTool` package [112]. This package uses the predictor-corrector method with Moore-Penrose corrector [110] (*apud* [112]) to compute equilibria, and the periodic orbits (and their stabilities) are computed via `AUTO` package, based on [113]. This `AUTO` package is a software for continuation and bifurcation problems in ordinary differential equations.

The maximum and minimum values of the angular velocity of the Disc 1 (R_1) is plotted when a periodic solution is found, while the normal force N_1 is kept constant. Figure 4.12 shows a supercritical Hopf bifurcation occurring at H_1; therewith, a stable periodic branch p_1 rises while an unstable equilibrium branch e_1 appears. In $\omega_{ref} = 2.9$ rad/s, there exists an unstable periodic branch p_2 and then a subcritical Hopf bifurcation occurs at H_2 ($\omega_{ref} = \omega_c = 1.994$ rad/s). From this point, a stable equilibrium branch e_2 rises. In addition, the points 1, 2 and 3 on the periodic branch p_1 were depicted in order to illustrate the torsional vibrations with stick-slip in the phase plane. One may notice that there is an angular velocity range of bi-stability, *i.e.*, the equilibrium and periodic solutions coexist. The system will perform either solution depending on the perturbation on it.

The normal force N_1 may be increased, and then the bifurcation diagram may be generated once again, as depicted in Figure 4.13. The analysis performed for Figure 4.12 may be applied. However, the ω_{min} and ω_c have changed. This latter now assumes $\omega_c = 2.689$ rad/s, *i.e.*, for $\omega_{ref} > 2.689$ rad/s an equilibrium branch e_2 rises. Nevertheless, one may notice that the angular velocity range of bi-stability is greater than that one in Figure 4.12.

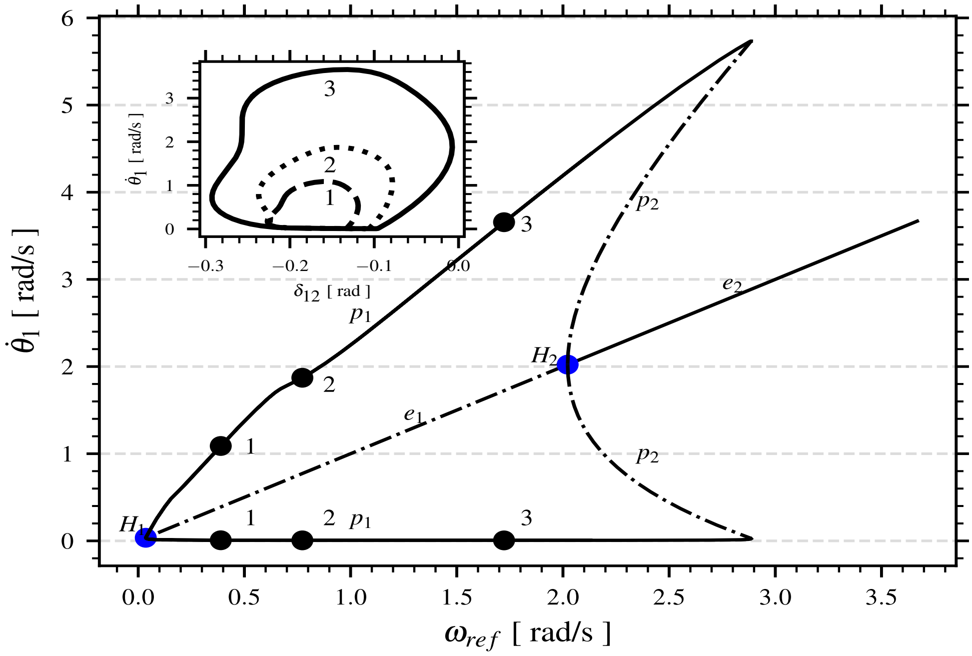

Figure 4.12: Numerical bifurcation diagram of the experimental set-up model with ω_{ref} as bifurcation parameter for $N_1 = 10.0$ N and $T_{r_2} = 0.0$ Nm. Continuous and dashed lines mean locally stable and unstable branches, respectively. The equilibrium branches are denoted as e_1 and e_2, whereas the periodic branches are denoted as p_1 and p_2.

4.5 Summary

The mathematical description of the drill-string experimental set-up was performed above. The lumped parameters technique was used to achieve this mathematical model (see Section 4.1). Thereafter, comparisons between experimental and numerical solutions in order to validate the mathematical model were employed in Section 4.2. Some non-modeled phenomena may influence the response of the system such as the temperature between the disc and pin. For example, it may increase the friction coefficients which herein were considered constants. Furthermore, manufacturing limitations imposed a slight rotation out of the plane of the disc R_1 and therewith variation in the normal force N_1 is observed. It is worth mentioning that the validation herein described was not fully performed. There are many techniques, which may include uncertainties or not, to perform a more detailed model validation depending on application requirements (see [83, 104, 114]).

The DC-motor dynamics was considered in the equations of motion, as described in Section 4.1. Once the DC-motor is not strong enough to provide the needed input torque, Section 4.3 presented its angular velocity oscillations

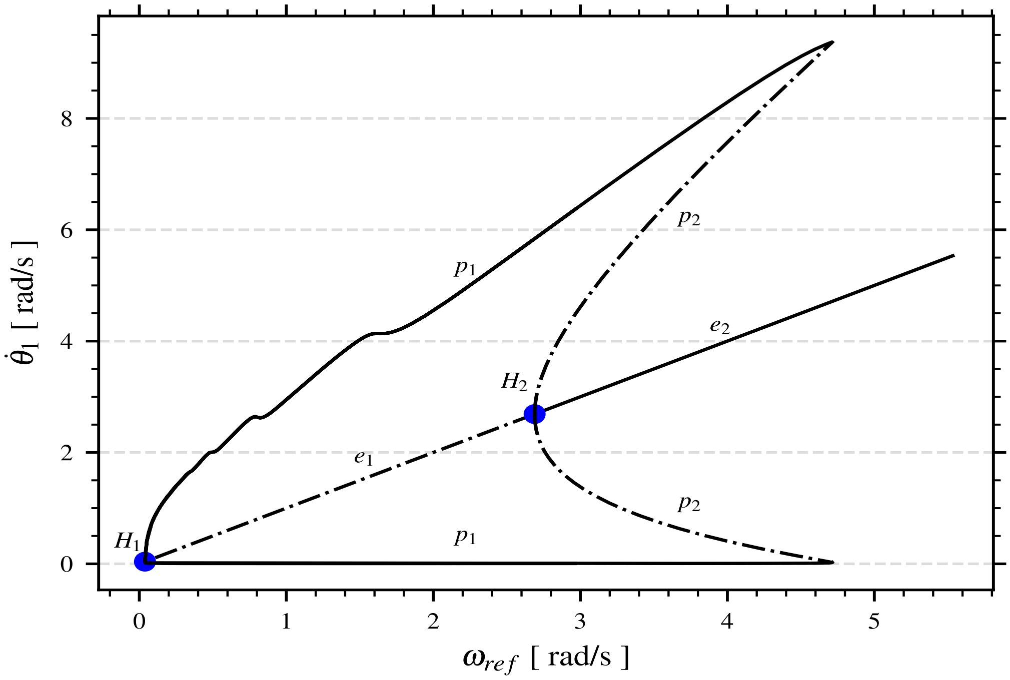

Figure 4.13: Numerical bifurcation diagram of the experimental set-up model with ω_{ref} as bifurcation parameter for $N_1 = 20.0$ N and $T_{r_2} = 0.0$ Nm. Continuous and dashed lines mean locally stable and unstable branches, respectively. The equilibrium branches are denoted as e_1 and e_2, whereas the periodic branches are denoted as p_1 and p_2

due to the transient state and the stick-slip phenomenon. The mathematical model did not depict the oscillation amplitudes but it oscillates nearly in the same frequency. On this point, an identification of the internal DC-motor parameters must be performed. Also, the numerical results of the armature current illustrates large oscillations during stick-slip in R_1. This fact proves the influence of one subsystem on the other, and then both must be considered. The armature current is not measured experimentally at present: it is the next step forward for a best description and comparison of the DC-motor dynamics.

The stability analysis of the system was performed in Section 4.4: in this section, first the stable and unstable equilibrium branches were identified. One may state that the friction model slope is substantially linked to the stability of the system solutions. In fact, some researchers show the system instability in a range of the bifurcation parameter equivalent to the negative slope of the friction model [44, 72]. Further, the system experiences a Hopf bifurcation: the critical value is a fixed point of the system; plus, an eigenvalue presents null real part at ω_c; and Real$(\mathrm{d}\lambda/\mathrm{d}\omega^*) \neq 0$ at $\omega^* = \omega_c$ - called the transversality condition [105, 107, 110]. The torsional vibration map was obtained via Hurwitz criterion where the curve shows two different regions: one region with stable periodic solutions and the other with stable equilibrium solutions. Moreover, the bifurcation diagrams were numerically obtained via a path-following technique provided by `PyDSTool` package: the reference angular velocity ω_{ref} was used as bifurcation parameter and the normal force N_1 was considered constant. One may verify that there is an angular velocity range in which stable periodic and equilibrium solutions coexist. This bi-stability behavior is later used for the mitigation strategy presented in next chapter.